Available online at www.sciencedirect.com
ScienceDirect
Aerospace Science and Technology 12 (2008) 485–489
Aerospace Science and Technology
www.elsevier.com/locate/aescte

Numerical study of the start-up process in an optimized rocket nozzle

José Antonio Moríñigo [a,*,1], José Juan Salvá [b,2]

[a] *Dpto. Programas Espaciales, Instituto Nacional de Técnica Aeroespacial, Ctra. Ajalvir km. 4, Torrejón de Ardoz, 28850 Madrid, Spain*
[b] *Dpto. Motopropulsión y Termofluidodinámica, ETSI Aeronáuticos, Universidad Politécnica de Madrid, Pza. Cardenal Cisneros 3, 28040 Madrid, Spain*

Received 14 September 2007; received in revised form 30 November 2007; accepted 30 November 2007

Available online 5 December 2007

Abstract

This work is to analyze the start-up process of the subscale optimized J2-S rocket nozzle by means of axisymmetric time-accurate Reynolds Averaged Navier–Stokes simulations. Specifically, the phenomena of the FSS → RSS transition (from fully separated to reattached flow), onset of backflow on the nozzle axis and opening of the separation bubble are investigated. Numerical predictions show a remarkable good agreement with experimental data. In particular, the FSS → RSS transition is correctly captured by axisymmetric modelling. The analysis of the flowfield across the shock pattern leads to a simple criterion for the FSS → RSS transition to occur. Furthermore, a mechanism and criterion for the appearance of backflow on the axis is suggested

Keywords: Backflow; FSS → RSS; Nozzle start-up; Restricted shock separation

1. Introduction

Various experimental and numerical studies have appeared in the literature concerning the complex phenomenology of Thrust Optimized Contour (TOC) nozzles. The first work on this topic is attributed to Nave and Coffey [12], who reported a hysteresis loop to occur for the subscale J-2S nozzle and the development of three different flow patterns: the fully separated flow or free shock separation (namely FSS), where the flow experiences shock-induced separation and does not reattach to the wall after separation; the restricted shock separation (RSS), where the flow is reattached with a separation bubble located after the separation shock; and the end-effect separation, which occurs when the separation bubble near the nozzle lip bursts and the flow is fully separated again. Chen et al. [2] carried out steady and transient numerical simulations for the subscale J-2S nozzle using a 2D Reynolds-averaged Navier–Stokes (RANS) solver with a modified Baldwin–Lomax turbulence model. They were able to capture the hysteric flowfield and the three flow patterns (fully separated flow with and without a large vortex just after the Mach disk; and the reattached flow pattern) for a wide range of Nozzle Pressure Ratios (NPRs). Their thrust efficiency results exhibit a rather encouraging agreement with the experiments of Nave and Coffey for the shutdown process, but they fail in the prediction of the start-up process.

This fact motivates in part the development of the present work. More recently, various experimental and numerical investigations focused on the transient operation of a variety of TOC nozzles with compressed [17] and parabolic [1,3,4,6–8,11,13] contour wall, have confirmed the appearance of multiple solutions and the role they play in side load generation. However, to the authors' knowledge, the numerical studies addressing the start-up process have failed to capture the FSS → RSS transition or the correct NPR value and these faulty predictions may be attributed to inaccuracies in the numerical method used.

The authors have performed 3D unsteady RANS simulations in the J-2S nozzle [10] for a set of NPRs and have shown the

* Corresponding author. Tel.: +34 91 520 1351, fax: +34 91 520 1384.
E-mail addresses: morignigoja@inta.es (J.A. Moríñigo), jjsalva@aero.upm.es (J.J. Salvá).
[1] Propulsion engineer, Dr.
[2] Professor, Member AIAA. Tel.: +34 91 3366347, fax: +34 91 3366375/71.

1270-9638/$ – see front matter
doi:10.1016/j.ast.2007.11.003

appearance of oscillating FSS → RSS transition at NPR = 43, which is in close agreement with the reported experimental FSS → RSS transition value [12]. Thus, in the present work, the start-up is analyzed following an identical numerical approach, but assuming axisymmetric flow since unsteady 3D simulations are highly demanding in terms of computing time (thus, side load generation is not captured by the present model). Specifically, this note revisits the start-up of the subscale TOC J2-S nozzle and addresses to capture the transition from fully separated to reattached flow, onset of backflow on the axis and opening of the separation bubble. The comparison between predictions and test data of Nave and Coffey shows a remarkable good agreement.

2. Numerical approach

Time-accurate simulations have been performed using a semi-discrete cell-centred parallel finite volume numerical code [9] which solves the 3D unsteady RANS equations on general body-fitted multi-block grids. Discretization provides 2nd-order accuracy in space and time. Gas is assumed ideal and Newtonian with laminar viscosity according to the Sutherland's law. Time integration is carried out with a 2nd-order implicit dual-time stepping scheme (physical time-step $\Delta t = 1$ ms and pseudo-time integration with multistage Runge–Kutta and Courant–Friedrichs–Lewy number CFL = 1.2). Artificial dissipation follows the classical Jameson–Schmidt–Turkel scheme. Turbulence is modelled with the two-equation k–τ linear eddy viscosity closure of Speziale et al. [15]. A turbulent stresses limiter has been implemented into the closure, yielding more realistic levels of turbulent kinetic energy across the shocks. Parallelization follows domain decomposition and message passing interface. More details on the implementation and validation in turbulent compressible flows may be found in Magagnato [9]. To deal with the axisymmetric simulations, the solver uses a slice domain with one cell set in the azimuthal direction, hence an axis boundary condition is imposed along the nozzle centreline.

Regarding the numerical boundary conditions, a stagnation temperature of 300 K and a time-varying pressure (p_c) have been prescribed at the nozzle air supply chamber. Chamber to ambient pressure ratio $p_c(t)/p_{amb}$ is increased from NPR = 10 to 72 (namely the range {10, 72}) with unitary staircase increments (ΔNPR) in {42,49} and ΔNPR = 2 elsewhere; the time elapsed at each NPR is 40 ms. Non-slip flow and adiabaticity are set at the walls. Static pressure $p_{amb} = 10^5$ Pa is prescribed far away at the external boundary (outflow condition) of the computational domain, that extends 20 nozzle exit radii streamwise and 10 radii in the radial direction, to minimize the effect of spurious reflections on the solution. A multiblock grid of 57,000 cells has been built with a first-cell clustered to the wall, to match the $y^+ \sim 1$ condition. Its adequacy to resolve the main flow features has been checked by a grid-independence study using finer and coarser grids obtained by doubling and halving, respectively, the number of grid lines of each coordinate direction.

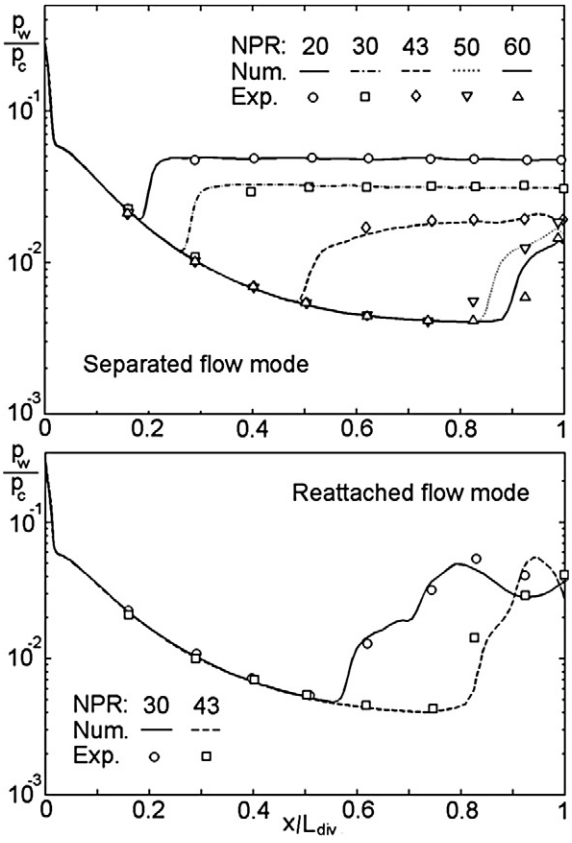

Fig. 1. Numerical-experimental comparison of pressure along the J-2S nozzle wall for the available NPRs data of the FSS and RSS modes. Wall pressure p_w has been non-dimensionalized with the chamber pressure p_c and axial position x with the nozzle divergent length L_{div}.

3. Results and discussion

3.1. Prediction assessment

The wall static pressure profiles have been compared with the experimental data of Nave and Coffey at NPR = 20, 30, 43, 50 & 60 for both fully separated and reattached flow modes (Fig. 1), showing a good agreement. The pressure bumps in Fig. 1b correspond to the succession of compression and expansion waves that evolves in the reattached flow region. It should be noted that the number of pressure taps on the wall impedes the precise determination of the separation point in the test. In addition, the close prediction of the computed separation with the Schmucker criterion [14] for a wide range of NPRs (for fully separated flow), reinforces the confidence on the simulation procedure.

Finally, the computed time-averaged thrust efficiency $C_E/C_{E,id}$ (computed to ideal thrust ratio, where ideal thrust corresponds to an isentropic expansion to the ambient at equal NPR) is depicted in Fig. 2 in the start-up from NPR = 10 to 72. The computed $C_E/C_{E,id}$ curve fits rather close to the experimental data, whereas Chen et al. computations overpredict the thrust efficiency in the whole start-up range and their flow structure corresponds to the fully separated flow. This overprediction seems to be attributed to the earlier separation captured in their

results. Furthermore, the thrust drop observed at the transition point ($2 \rightarrow 3$) is correctly predicted at about the reported NPR in the present work.

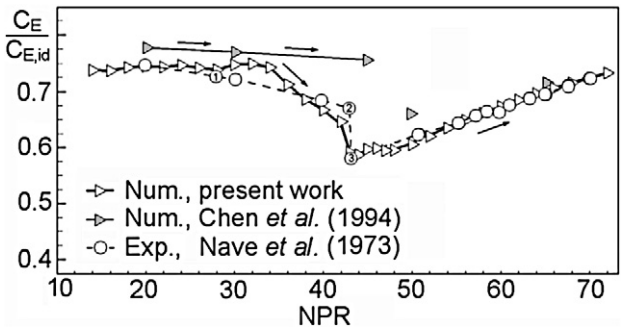

Fig. 2. Thrust efficiency $C_E/C_{E,id}$ of the J2-S nozzle, where $C_E/C_{E,id}$ is time-averaged within each NPR-staircase interval of 40 ms during the start-up. Numerical results of Chen et al. [2] are also included for comparison.

3.2. Flow structure and analysis

Fig. 3 illustrates the flow structure in the NPR-interval $\{42, 47\}$ where the FSS $\rightarrow$ RSS transition occurs. The snapshot NPR $= 42$ shows the existence of an incipient cap-shock pattern, formed by a Mach disk (MD); a cap-shaped shock (CSS) running from the triple point T_i to the annular Mach Disk (AMD); a separation shock (SS); and the two reflected shocks (RS) at the triple points T_{up}, T_{dw} set at the ends of the AMD.

Moreover, a two coaxial-jet structure due to the cap-shock is here apparent, namely a subsonic inner-jet and an annular supersonic outer-jet. Furthermore, from NPR $= 42$ on, two vortical structures at both sides of the outer-jet arise: one in the separated flow region; and the other trapped between the inner- and outer-jet, made up of a pattern of evolving vortices. These structures add fluctuations to the flowfield. The examination of the NPR sequence in Fig. 3 leads to identifying the FSS $\rightarrow$ RSS transition occurring at NPR ~ 43, in remark-

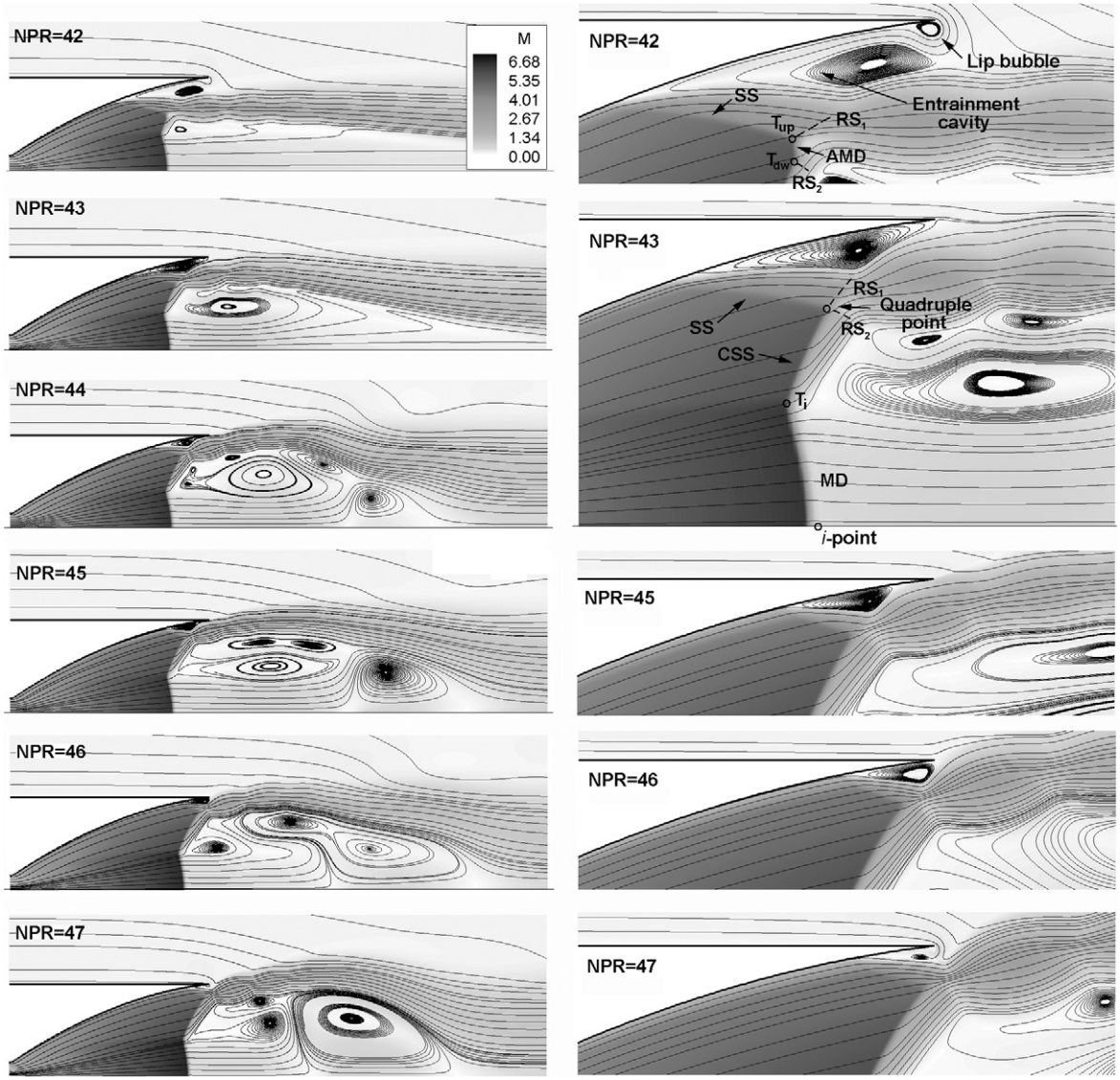

Fig. 3. Sequence of Mach field snapshots with overlaid instantaneous streamlines, corresponding to the NPR interval $\{42, 47\}$ of the J2-S nozzle start-up. The views on the right side zoom the separation bubble region and cap-shock pattern under the wall.

able agreement with the experiments. The results show that the computed $C_E/C_{E,id}$ plotted in Fig. 2 exhibits an abrupt decay ($C_E/C_{E,id} \to 0.59$) near NPR = 43, whose origin is attributed to the FSS → RSS transition according to the wall pressure profiles. It is observed that in the process of reattachment, a large forward movement of the separation point takes place. At NPR = 44 a large recirculating flow region on the axis is clearly seen, which will be addressed in the next subsection. The flow remains reattached (RSS mode) from NPR = 43 to 47 and finally separates again when the separation bubble reaches the nozzle lip at about NPR ∼ 47; then the separation bubble bursts and the fully separated flow is recovered.

The flow complexity makes it difficult to state a quantitative criterion to predict the FSS → RSS transition. To this respect, Frey and Hagemann [5] have pointed out the role of the cap-shock pattern to drive the outer-jet direction. Furthermore, their semi-analytical model, out of momentum flux considerations, has provided good predictions in the nozzles analyzed. Thus, appealing results are obtained with an adequate empirical and simulation-based calibration.

A qualitative explanation of the transition from fully separated to reattached flow may be given by analyzing the role played by the shocks and the separated region on the direction of the outer-jet. Basically, the elements that drive the direction of the outer-jet are the CSS, which redirects the outer-jet axis towards the wall (then increasing the angle of the outer-jet with the nozzle axis); the AMD, that leaves an almost axial flow; the SS which turns the flow towards the axis; and the entrainment cavity under the wall, where the overall static pressure decreases with NPR as the inflow velocity increases due to the stretching of the cavity entrance as the outer-jet approaches the nozzle lip.

The AMD counteracts the upward deflection imparted by the CSS while it dominates over CSS. A closer examination of Fig. 3 reveals that the flow reattaches once the AMD has disappeared and then the SS and CSS intersect each other in a quadruple point. This finding constitutes an interesting behaviour as the absence of the AMD favours the outer-jet deflection towards the wall. It should be note that the formation of an AMD is case dependent (linked to the wall contour geometry and gas properties), which explain that the AMD is not discernible in some reported numerical studies [4,6]. In particular, Chen et al. present a similar shock pattern in the final state solution of their impulsive simulation conducted for NPR = 45.

For some NPR within {42, 43} the deflection of the outer-jet towards the wall favours the external shear layer of the outer-jet to merge with the shear layer of the small bubble anchored to the nozzle lip, closing the entrainment path. Hence, the FSS → RSS transition follows. This behaviour suggests that transition occurs upon the fulfilment of two flow conditions: the axis of the outer-jet should be deflected towards the wall; and the outer-jet boundary must intercept it. Thus, a simple criterion can be established, that is the FSS → RSS transition will take place when the angle of the flow at the quadruple point be equal or greater than the nozzle lip angle. Fig. 3 shows that the second condition is not satisfied for NPR > 46 as the further location of the SS (close to the lip) impedes now the reattachment.

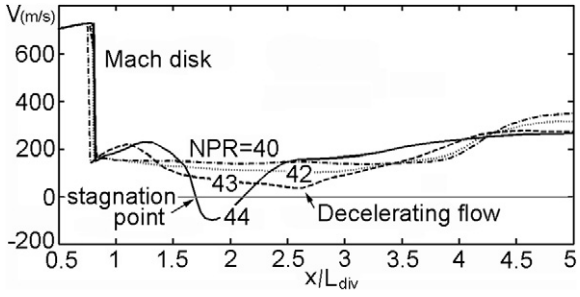

Fig. 4. Time-averaged velocity profile along the nozzle axis for NPR = 40, 42, 43, and 44. The decelerating flow zone at NPR = 43 is indicated.

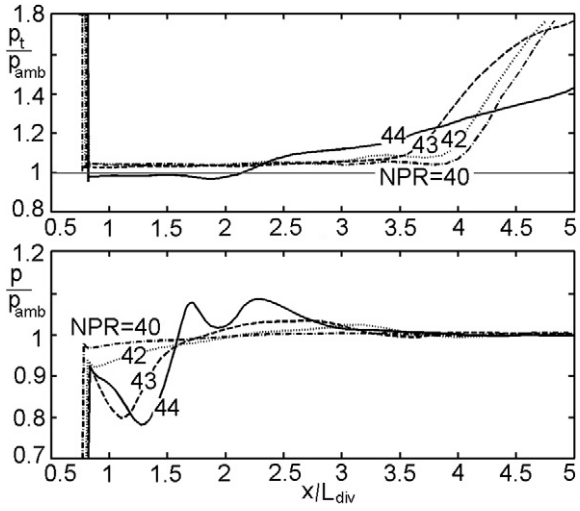

Fig. 5. Time-averaged stagnation and static pressure profiles at the nozzle axis for NPR = 40, 42, 43 and 44.

3.3. Onset of backflow on the axis

The onset and evolution of backflow on the nozzle axis is illustrated in Fig. 3. Once backflow arises, a large recirculation region appears, delimited by leading and rear stagnation points. This recirculating flow is clearly seen for NPR = 44. Moreover, an examination of the flowfield at the axis after the MD (see Figs. 4 and 5) reveals that the static pressure increases towards the farfield pressure, so the flow is decelerated to a minimum velocity value. After this zone, the axial static pressure gradient becomes negligible and the flow is accelerated by the shear action of the outer-jet. As the minimum velocity value decreases with NPR, it is plausible to imagine that for certain NPR = NPR* within {43, 44} a single stagnation point is set on the axis, such that when NPR > NPR* backflow develops and a recirculation region grows with NPR. In a strict sense, the inherent fluctuations of the flow will favour the cyclic formation and collapse of a very small recirculation region instead of the ideal single stagnation point here introduced from a conceptual standpoint. Hence, the critical NPR* separates two flow regimes: with or without recirculating flow on the axis.

In addition to this qualitative description, a criterion to predict the onset of backflow may be suggested from the analysis of the computed flowfield downstream the MD. Basically, the flow along the axis between the i-point (see Fig. 3) and the m-

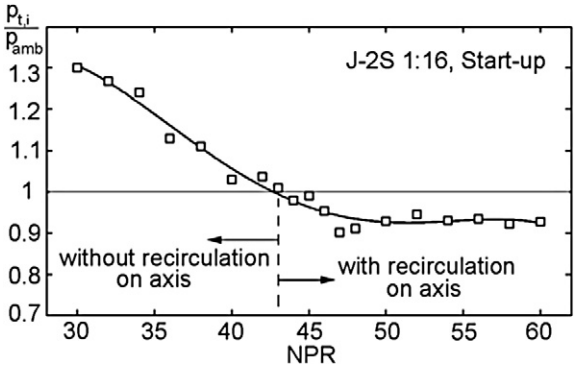

Fig. 6. Stagnation to ambient pressure ratio $p_{t,i}/p_{amb}$ at the axis, ahead of the Mach disk (i-point) during the start-up (□: instantaneous data, —: 4th-order polynomial fitting).

point of minimum velocity at the axis is near isentropic since viscous dissipation is small in this zone. Furthermore, the static pressure in the core of the inner-jet experiences a rapid adaptation to the farfield pressure p_{amb}, as can be seen in Fig. 5, then the pressure at the point of minimum velocity (p_m) satisfies $p_m \sim p_{amb}$. Under these assumptions we can write

$$\frac{p_{t,i}}{p_{amb}} \approx \left(1 + \frac{\gamma - 1}{2} M_m^2\right)^{\frac{\gamma}{\gamma-1}}$$

Consequently, the onset of recirculation should occur when $p_{t,i} < \sim p_{amb}$ is fulfilled. In this way, as NPR increases the MD moves downstream, $p_{t,i}$ decreases and also M_m, hence, backflow arises as soon as $p_{t,i}$ reaches p_{amb} and the critical NPR becomes determined. To test this criterion, $p_{t,i}/p_{amb}$ has been computed with

$$\frac{p_{t,i}}{p_{amb}} = \frac{p_{t,i}}{p_c}\frac{p_c}{p_{amb}} \approx f(M_{up}) \cdot \text{NPR}$$

where M_{up} is the Mach number before the MD at the nozzle axis and

$$f = \left[1 + \frac{2\gamma}{(\gamma+1)}\left(M_{up}^2 - 1\right)\right]^{1/(\gamma-1)} \cdot \left[\frac{(\gamma+1)M_{up}^2}{(\gamma-1)M_{up}^2 + 2}\right]^{\gamma/(\gamma-1)}$$

The evolution of the ratio $p_{t,i}/p_{amb}$ during the start-up versus NPR is plotted in Fig. 6, showing that the NPR* corresponding to $p_{t,i}/p_{amb} \sim 1$ agrees well with the onset value (NPR $\sim$ 43) inferred from Figs. 4 and 5. The Mach field sequence illustrates the growing of the recirculating flow with NPR and its location far from the shock pattern. It should be said here that this location resembles some recent results obtained by other authors in TOC nozzles [1,3,7,17] but differs from Chen et al., who showed a large backflow bubble anchored just after the cap-shock. Controversy on the real existence of the backflow has been finally clarified after its empirical confirmation [16].

4. Conclusions

Flow reattachment and onset of recirculation on the nozzle axis at the start-up process have been investigated by means of axisymmetric time-accurate simulations. Results stress that FSS → RSS transition is well captured by axisymmetric modelling and exhibits good agreement with the experimental data. The analysis of the flowfield across the cap-shock pattern leads to establishing a simple and necessary condition for the FSS → RSS transition. Furthermore, a mechanism and criterion for the appearance of backflow on the axis has been addressed for the nozzle considered. Nevertheless, three-dimensional simulations are needed to explore in detail the unclear aspects linked to the fluctuating, asymmetrical nature of the flow. Hence, further research is in progress.

Acknowledgements

The first author thanks F. Magagnato of the Technical University of Karlsruhe for making available his solver. Access to computational resources of the Instituto Nacional de Técnica Aeroespacial (INTA) and Centro de Investigaciones Energéticas, Medioambientales y Tecnológicas (CIEMAT) is acknowledged.

References

[1] T. Alziary de Roquefort, Unsteadiness and side loads in over-expanded supersonic nozzles, in: Proc. 4th European Symp. Aerothermodynamics for Space Vehicles, ESA SP-487, Capua, Italy, 2001.
[2] C.L. Chen, S.R. Chakravarthy, C.M. Hung, Numerical investigation of separated nozzle flow, AIAA J. 32 (9) (1994) 1836–1843.
[3] S. Deck, A.Th. Nguyen, Unsteady side loads in a thrust-optimized contour nozzle at hysteresis regime, J. Propulsion and Power 42 (9) (2004) 1878–1888.
[4] M. Frey, G. Hagemann, Restricted shock separation in rocket nozzles, J. Propulsion and Power 16 (3) (2000) 478–484.
[5] M. Frey, G. Hagemann, Flow separation and side-loads in rocket nozzles, AIAA Paper 99-2815, 1999.
[6] M. Frey, G. Hagemann, Status of flow separation prediction in rocket nozzles, AIAA Paper 98-3619, 1998.
[7] A. Groß, C. Weiland, Numerical simulation of separated cold gas nozzle flows, J. Propulsion and Power 20 (3) (2004) 509–519.
[8] G. Hagemann, M. Frey, W. Koschel, Appearance of restricted shock separation in rocket nozzles, J. Propulsion and Power 18 (3) (2002) 577–584.
[9] F. Magagnato, KAPPA – Karlsruhe parallel program for aerodynamics, Task Quarterly(2) (1998) 215–270.
[10] J.A. Moríñigo, J.J. Salvá, Three-dimensional simulation of self-oscillating flow and side-loads in an overexpanded subscale rocket nozzle, J. Aerospace Engineering 220 (5) (2006) 507–523.
[11] F. Nasuti, M. Onofri, Viscous and inviscid vortex generation during startup of rocket nozzles, AIAA J. 36 (5) (1998) 809–815.
[12] L.H. Nave, G.A. Coffey, Sea level side loads in high-area-ratio rocket engines, AIAA Paper 73-1284, 1973.
[13] M. Onofri, F. Nasuti, The physical origins of side loads in rocket nozzles, AIAA Paper 99-2587, 1999.
[14] R. Schmucker, Strömungsvergänge beim Betrieb über-expandierter Düsen chemischer Raketentriebwerke, TU Munich, Report TB-7,-11,-14, Munich, July 1973.
[15] C.G. Speziale, R. Abid, E.C. Anderson, A critical evaluation of two-equation models for near wall turbulence, ICASE Report No. 90-46, 1990.
[16] R. Stark, W. Kwan, F. Quessard, G. Hagemann, M. Terhard, Rocket nozzle cold-gas test campaigns for plume investigations, in: Proc. 4th European Symp. Aerothermodynamics for Space Vehicles, ESA SP-487, Capua, Italy, 2001.
[17] M. Takahashi, S. Ueda, T. Tomita, H. Tamura, K. Aoki, Transient flow simulation of a compressed truncated perfect nozzle, AIAA Paper 2001-3681, 2001.